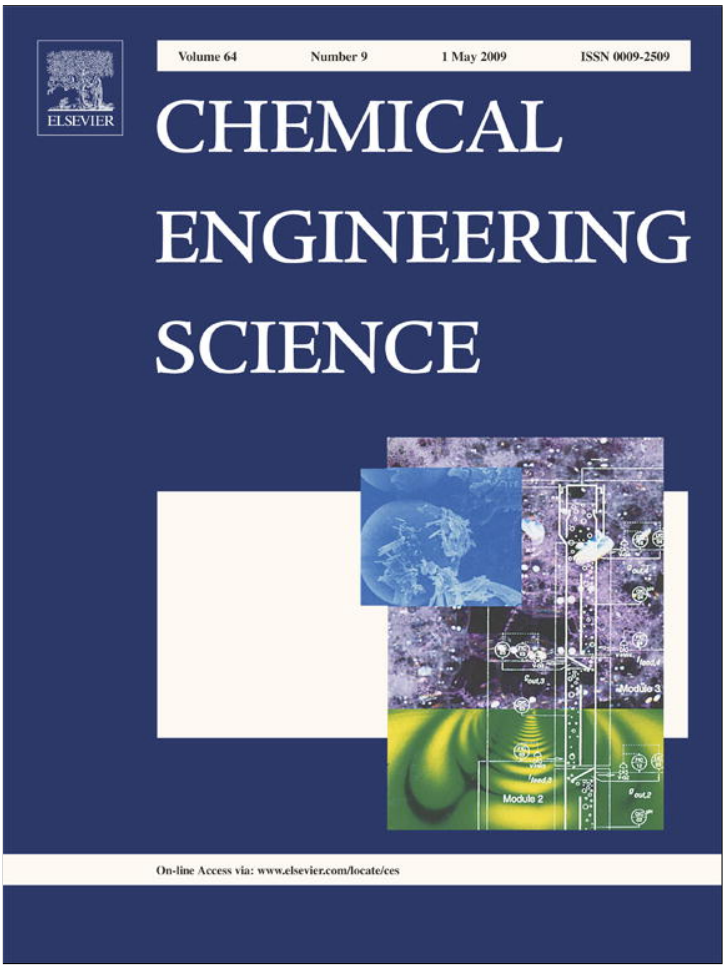

Chemical Engineering Science 64 (2009) 1953 – 1967

Contents lists available at ScienceDirect

Chemical Engineering Science

journal homepage: www.elsevier.com/locate/ces

Bacterial aerosol neutralization by aerodynamic shocks using a novel impactor system: Design and computation

P.R. Sislian[a], X. Zhang[a], M. Li[b], D. Pham[a], L. Mädler[c], P.D. Christofides[a,d,*]

[a]Department of Chemical and Biomolecular Engineering, University of California, Los Angeles, CA 90095, USA
[b]Department of Chemical and Materials Engineering, California State Polytechnic University, Pomona, CA 91768, USA
[c]Foundation Institute of Materials Science, Department of Production Engineering, University of Bremen, Badgasteiner Str. 3, 28359 Bremen, Germany
[d]Department of Electrical Engineering, University of California, Los Angeles, CA 90095, USA

ARTICLE INFO

Article history:
Received 25 September 2008
Received in revised form 14 December 2008
Accepted 13 January 2009
Available online 28 February 2009

Keywords:
Bacterial aerosol
Aerodynamic shocks
Impactors
Process modeling
Computation
Particle motion

ABSTRACT

Neutralization of bacterial aerosol releases is critical in countering bioterrorism. As a possible bacterial aerosol neutralization method that avoids the use of chemicals, we investigate the mechanical instabilities of the bacterial cell envelope in air as the bacteria pass through aerodynamic shocks. To carry out this fundamental investigation, a novel experimental impactor system is designed and built to simultaneously create a controlled and measured shock and to collect the bacteria after they pass through the shock. In the impactor system the aerosol flows through a converging nozzle, perpendicular to a collection surface that has an orifice through which the shocked bacteria enter the deceleration tube. Both experimental measurements of the pressure in the impactor system at multiple points and computational fluid dynamics simulations are used to quantitatively characterize the shocks created in the impactor. Specifically, the developed computational model describes the evolution of both the gas and the particle velocity and temperature in the impactor system to determine the forces exerted on the bacterial aerosol as they pass through the shock. The results indicate that the developed computational model predictions compare well with the experimental pressure measurements. The computational model is also used to predict the magnitude of the acceleration needed to neutralize various bacterial aerosols and guide on-going experimental work.

1. Introduction

Natural bacterial aerosol is present both in indoor and in outdoor environments at background concentrations. The suspended bacterial particles usually range in size from 1 μm (single cells) to 10 μm (multiple cells or cells associated with debris) (Vitko, 2005). With respect to bioaerosol concentrations, the comparison of concentration data from different environments is, in general, very difficult. For outdoor environments, the reported literature values of bioaerosol concentration range from 80 cfu/ml in rural areas (Bovallius et al., 1978; Jones and Cookson, 1983; Shaffer and Lighthart, 1997; Tong and Lighthart, 1999) to 850 cfu/ml in urban areas (Bovallius et al., 1978; Di Giorgio et al., 1996; Lighthart and Shaffer, 1997; Mancinelli and Shulls, 1978), where cfu refers to colony forming units. Indoor environments usually contain less bioaerosol. Different sources contribute to the background in different environments such as soil, water, plants and human activity (anthropogenic aerosol).

In addition to bioaerosols present in indoor and outdoor environments at background concentrations, intentionally produced anthropogenic bacterial aerosols can potentially be used as bioterrorism agents, which are added to natural background concentrations. Assuming that detection of these agents is possible, effective neutralization is necessary to minimize human casualties (Vitko, 2005). Current methods are not effective in neutralizing the aerosol cloud at its source and mostly include containment of the aerosol release in order to minimize human exposure. These methods are limited to indoor environments and employ techniques such as high efficiency particulate air (HEPA) filtration, electrostatic precipitation, steam condensation, ultraviolet (UV) inactivation as well as diverting airflows (Vitko, 2005).

The use of aerodynamic shocks holds promise as an alternative way to neutralize the bacterial aerosol at the source. The shock can be applied at the point of release both in indoor and in outdoor air with the advantage of avoiding chemicals. Some experimental data exist in the literature (Horneck et al., 2001; Lundbeck and Skoldber, 1963;

* Corresponding author at: Department of Chemical and Biomolecular Engineering, University of California, Los Angeles, CA 90095, USA. Tel.: +1 310 794 1015; fax: +1 310 206 4107.
E-mail address: pdc@seas.ucla.edu (P.D. Christofides).

0009-2509/$ - see front matter © 2009 Elsevier Ltd. All rights reserved.
doi:10.1016/j.ces.2009.01.021

Teshima et al., 1995) on the use of shock waves to neutralize bacteria; however, these studies are limited to liquid bacterial suspensions or powders and do not assess the effects of a shock in the aerosol phase. We aim at understanding the fate of the bioaerosol particles when exposed to shocks of different velocity, temperature and pressure gradients in air.

Although detailed data for the effect of shocks on bioaerosol particles are lacking, shock waves have been shown to cause lysis of bacteria suspended in the liquid phase (Lundbeck and Skoldber, 1963; Teshima et al., 1995). Teshima et al. (1995) studied the biomechanical effects on *E. coli* by attaching a test tube with the bacterial suspension at the end of a shock tube. The peak pressure of the shock was varied from 3 to 14 MPa with 100 pulses and bacterial lysis was quantified by measuring leaked phenylalanine dehydrogenase activity (Teshima et al., 1995). At 14 MPa, 15% of the *E. coli* cells were destroyed (Teshima et al., 1995). The researchers mentioned the importance of the pulse width but failed to account for its effect (Teshima et al., 1995). In earlier studies, Lundbeck and Skoldber (1963) used a shock peak pressure of ≈ 6 MPa with a variable number of pulses to neutralize bacteria suspended in the liquid phase. The shocks were produced using a piston fitted to a stainless steel tube filled with suspension. The study showed a loss of viability of *E. coli* vegetative cells but did not show any significant effect on *B. subtilis* spores (Lundbeck and Skoldber, 1963). The authors also demonstrated that an increase in concentration results in an increase of bacterial viability. Our approach to shock bioaerosol particles in an impactor system avoids the concentration effect because individual cells pass through the shock; this allows understanding of the mechanism of single bacterial lysis by an aerodynamic shock.

More recently, Horneck et al. (2001) showed that only 0.01% of dried *B. subtilis* powder (mounted between two quartz plates) survived a shock peak of 32 GPa with 1 pulse. However, the temperature of the cells in the sample reached 250 °C (Horneck et al., 2001) and it was not possible to separate the effect of the shock from that of temperature.

Based on the previous studies reported in the literature, we have designed and built an experimental impactor system capable of simultaneously creating a well-defined shock and collecting bacterial aerosol with very small velocity (< 10 m/s) at the point of impaction (Stewart et al., 1995). In the impactor system the aerosol flows through a converging nozzle, perpendicular to a collection surface. The collection surface has an orifice through which the shocked bacteria enter a deceleration tube where their velocity is reduced to avoid neutralization by impaction. The present work focuses on the development of a computational gas (flow and temperature) and particle motion model for the impactor system capable of predicting the effect of the shock on the bacterial aerosols. Experimental pressure measurements provide information about the flow field in the impactor and are compared with computational model predictions. Sharp changes in velocity, temperature and pressure across the shock induce instabilities on the bacterial membrane. The magnitude of the deceleration of the bacterial particle is calculated and is compared with theoretical values needed for the neutralization of different bacteria.

2. Design of the impactor system

The impactor system consists of a plate designed for the collection of the bacterial aerosol (see Fig. 1; parts 2 and 3) which is placed perpendicular to the gas flow emerging from a converging nozzle (see Fig. 1; part 1). Isentropic flow theory of an ideal gas predicts a critical downstream (P_1) to upstream (P_0) pressure ratio below which the flow at the exit of the nozzle is sonic (Liepmann and Roshko, 2001; Shapiro, 1953), according to the following equation:

$$\chi_{crit} = P_1/P_0 = [2/(\gamma+1)]^{\gamma/(\gamma-1)}, \tag{1}$$

where γ is the heat capacity ratio ($\gamma = 1.4$; $\chi_{crit} = 0.53$ for air). The generated impinging flow on a plate from a converging nozzle operating under sonic conditions results in the creation of a standoff shock whose properties can be changed by varying impactor geometry and operating conditions (Alvi et al., 2002; Delamora et al., 1990a,b; Jurcik et al., 1989; Powell, 1988). In traditional impactors (Hering et al., 1978, 1979), the aerosol is collected by impaction on a flat surface. Stewart et al. (1995) showed that bacteria collected by impaction are injured; therefore, assessing damage induced by the standoff shock is impossible using current impactor designs. To avoid loss of viability by impaction, the flat surface of the developed impactor system has an opening (see Fig. 1; part 2) that acts as a virtual surface through which the bacteria enter a stagnant gas deceleration tube (see Fig. 1; parts 2 and 3). Biswas and Flagan (1988) have designed a similar tube to prevent particle re-entrainment (Biswas and Flagan, 1988). The final velocity of the bacterium is related to the length of the tube (δl) and is calculated, assuming that the air in the deceleration tube is stagnant, using a force balance of the form:

$$m_p \frac{dv_p}{dt} = m_p v_p \frac{dv_p}{dx} = F_D + m_p g, \tag{2}$$

the drag force F_D is given by the Stokes–Cunningham law as follows:

$$F_D = \frac{-3\pi\mu d_p v_p}{C_c}, \tag{3}$$

where m_p is the bacterium mass, v_p is the bacterium velocity, d_p is the bacterium diameter, x is the axial coordinate, g is the gravitational constant, and μ is the dynamic viscosity of the gas. C_c, the Cunningham slip correction factor, accounts for non-continuum effects (for 1 μm particles $C_c = 1.164$ (Friedlander, 2000)). The length of the deceleration tube $\delta l = (C_c m_p v_{p|x})/(3\pi\mu d_p)$ is obtained by integrating Eq. (2) (neglecting the effect of gravity) between the tube inlet ($x' = x$) and the impaction surface at the end of the deceleration tube ($x' = \delta l + x$). The length of the tube, δl, varies between 1 and 4 mm in the impactor design of Fig. 1, which is sufficient to collect 1 μm particles entering the deceleration tube at velocities ($v_{p|x}$) up to 680 m/s. The bacterium experiences deceleration both as it passes through the shock and in the boundary layer of the plate; therefore, a tube between 2 and 4 mm in length is sufficient to collect bacteria at negligible velocities. More detailed computational modeling of the impactor system (see Section 4) confirms that the bacterium velocity at the entrance of the deceleration tube ($v_{p|x}$) is much smaller than $v_{p|x} = 680$ m/s which is assumed in the design of the deceleration tube. A detailed solution of Eqs. (2) and (3), without the assumption of stagnant gas, reveals low impaction velocities (< 10 m/s) at the point of collection (see Section 4).

The deceleration tube (see Fig. 1; parts 2 and 3 combined) is held on a support (see Fig. 1; part 5). The distance between the opening of the deceleration tube and the nozzle outlet (x) can be adjusted with spacers of different thickness (see Fig. 1; part 4). The exit chamber (see Fig. 1; part 6) has two outlets (see Fig. 1; part 7); one outlet connects to a vacuum pump and the other connects to a pressure gauge for Pitot measurements. The upstream pressure (P_0) and the downstream pressure (P_1) are measured through small orifices drilled normal to the side walls of the converging nozzle and of the exit chamber, respectively (see Fig. 1; part 7). A valve attached to a purge stream downstream of the impactor controls P_1, whereas a nitrogen tank with a pressure regulator controls P_0.

Depending on the method of analysis, different collection substrates can be placed on the top surface of the screw (see Fig. 1; part 3) to collect the shocked bacteria. A silicon wafer substrate is used

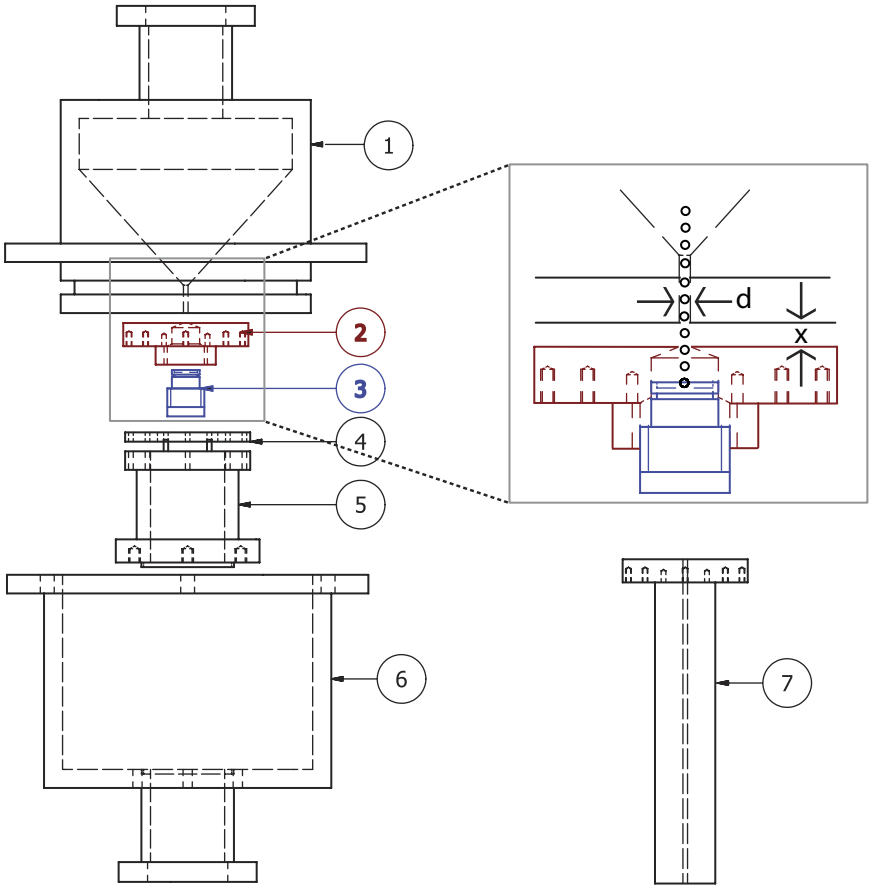

Fig. 1. Schematic of the impactor system: (1) converging nozzle with an exit diameter of either 0.5 or 1 mm, (2) and (3) a flat surface with a 0.5 or 1 mm hole combined with a screw that accommodates the collection substrate make up the deceleration tube (these parts can be replaced with a Pitot tube to measure the stagnation pressure), (4) spacers allow variation of the plate to nozzle distance from 0 to 2 mm, (5) support holding the deceleration tube and flat surface at fixed distance from the nozzle, (6) exit chamber, and (7) Pitot tube which can replace parts 2 and 3 for stagnation pressure measurements.

for scanning electron microscopy (SEM) and a copper grid is used for transmission electron microscopy (TEM). Both analysis techniques reveal qualitative structural data of the collected samples. Biochemical analysis can also be carried out by placing a black polycarbonate filter on the top surface of the screw (see Fig. 1; part 3), which is stained during post processing using a LIVE/DEAD® *Bac*Light™ (cat. number L7012; Life Technologies Corporation) to assess the viability of the collected bacteria, both quantitatively and qualitatively. Experimental results and analysis of the collected bacteria are the subject of another work.

Parts 2 and 3 can be replaced with a Pitot tube that has the same diameter opening as the deceleration tube (0.5 or 1.0 mm). The Pitot tube extends beyond the support and exit chamber (see Fig. 1) and is connected to a pressure gauge that measures the stagnation pressure. The alternate Pitot setup, similar to the ones used in previous studies (Donaldson and Snedeker, 1971; Scroggs and Settles, 1996), allows experimental characterization of the standoff shock (see Section 3.1). The developed system therefore has the advantage of passing the bacteria through a controlled and measured aerodynamic shock and simultaneously collecting them on various substrates for further analysis. The simultaneous detection eliminates the need to sample the bacterial aerosol compared to shock tube geometries, thereby reducing sampling errors. Both the operating pressures (P_0 and P_1) and the geometry of the impactor (nozzle diameter, d, and plate to nozzle distance, x) affect the properties of the aerodynamic shock (Delamora et al., 1990a,b). Their effect will be quantitatively studied.

3. Experimental and computational studies of the impactor system

The velocity, pressure, and temperature of the gas in the impactor system for different geometric and operating conditions are important parameters in determining the forces that act on a bacterium as it passes through the aerodynamic shock. Experimental measurements are compared with computational fluid dynamics (CFD) model predictions. CFD calculations provide velocity, pressure and temperature data at every point in the impactor system which are not accessible in the experimental impactor system. The CFD profiles are also used to predict the particle velocity and temperature in the impactor system (see Section 4). Therefore, comparison of the experimental and computational data provides realistic predictions of the eventual fate of different bacterial particles as they pass through the shock and are collected in the system.

3.1. Experimental results: Pitot pressure measurements

One of the directly measured variables in the experimental impactor system of Fig. 1 (see Section 2) is the Pitot stagnation pressure (P_p) after the shock. While a detailed CFD model has been developed for the experimental impactor system (see Section 3.2), in order to be able to compare our experimental measurements with results available in the literature, we first develop an impactor model based on appropriate simplifying assumptions to estimate the Mach

number before the shock (M_1) using the Pitot pressure measurement (P_p) along with that of upstream (P_0) and downstream (P_1) pressures.

Specifically, the gas is considered to be thermally perfect (i.e., the enthalpy (h) is only a function of temperature; $h = h(T)$) and calorically perfect (i.e., the heat capacity (c_p) at constant pressure is not a function of the temperature; $c_p \neq c_p(T)$). Along the center streamline, the flow before and after the shock is assumed to be one dimensional, steady-state and isentropic (i.e., adiabatic and frictionless). These conditions lead to $p_{01} \approx P_0$ and $p_{02} \approx P_p$, where p_{01} and p_{02} are the stagnation (or total) pressures before and after the shock, respectively. Both P_0 and P_p are experimentally measured in our system (see Section 2). The flow through a shock is non-isentropic ($p_{01} \neq p_{02}$; i.e., not in equilibrium). Assuming that the shock is infinitely thin and normal to the center streamline, the following equation can be used to relate the stagnation pressures to the Mach number before the shock (Liepmann and Roshko, 2001; Shapiro, 1953):

$$\frac{P_p}{P_0} \approx \frac{p_{02}}{p_{01}} = \left[1 + \frac{2\gamma}{\gamma+1}(M_1^2 - 1)\right]^{-1/(\gamma-1)} \left[\frac{(\gamma+1)M_1^2}{(\gamma-1)M_1^2 + 2}\right]^{\gamma/(\gamma-1)}, \quad (4)$$

where γ denotes the heat capacity ratio and M_1 is the Mach number before the shock. The Mach number after the shock (M_2) can also be calculated using M_1 under the above flow assumptions using the following formula (Liepmann and Roshko, 2001; Shapiro, 1953):

$$M_2^2 = \frac{1 + \frac{\gamma-1}{2}M_1^2}{\gamma M_1^2 - \frac{\gamma-1}{2}}, \quad (5)$$

Although the experimental pressure measurements do not provide a detailed picture of the flow field in the impactor, one can use the Mach number before the shock as a measure of the velocity change ($M_1 - M_2$) over the thickness of the shock which can be estimated to be on the order of one mean free path (λ) of the gas, which is given by (Clift et al., 1978):

$$\lambda = 2.15\mu T_{01}^{1/2}/P_{01}, \quad (6)$$

where T_{01} and P_{01} are the static temperature and pressure before the shock, respectively. The Mach number combined with the shock thickness is important in determining the forces exerted on the bacterial particles (see Sections 4 and 5).

The flow-field assumptions used in the derivation of Eqs. (4) and (5) give rise to errors in determining the actual shock Mach number. Detailed CFD simulations (see Section 3.2) can be used to compute a better estimate of the Mach number and will therefore be used in the development of a bacterial particle break-up model (see Sections 4 and 5). Nonetheless, the experimental Pitot measurements constitute a basis for comparison with both experimental data found in the literature and with the CFD simulations. The experimental impactor systems found in the literature are geometrically different from the impactor system of Fig. 1 (Donaldson and Snedeker, 1971; Powell, 1988; Scroggs and Settles, 1996). Although impactor system geometry is an important factor that affects the flow characteristics of the impinging jet, a comparison is still useful if the objective is to determine whether the two sets of measurements (Pitot pressure) or calculations (Mach number) fall within the same range. Therefore, even when the operating conditions are the same, we do not expect the measurements and calculations to agree perfectly.

Specifically, Powell (1988) calculated an oscillating Mach number as a function of the distance between the nozzle and the Pitot tube, x/d. Measurements with the current system (see Fig. 1) were carried out to mimic Powell's operating conditions ($P_0 = 3.72$ atm and $P_1 = 1$ atm) (Fig. 2). However, the geometries differ as follows: (1) $d = 7.9$ mm in Powell (1988) setup compared with $d = 0.5$ mm in the impactor system of Fig. 1, and (2) a Pitot tube of unspecified geometry without the flat plate is used in Powell's case (Powell, 1988),

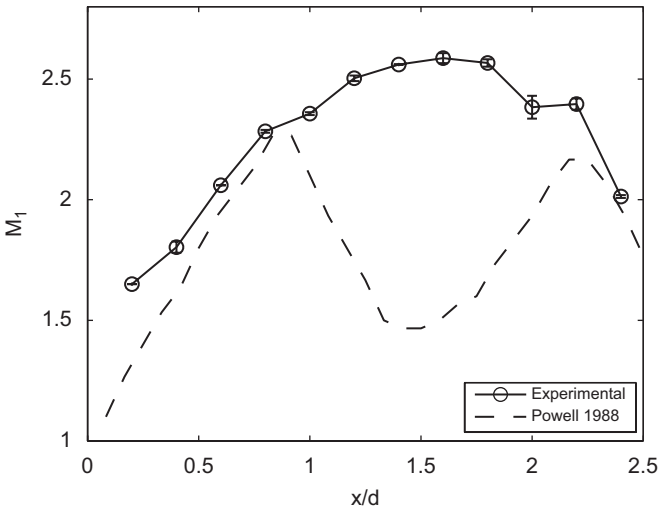

Fig. 2. Experimental Mach number before the shock (M_1) calculated using Eq. (4) compared to measurements from Powell (1988). M_1 is plotted as a function of x/d. The operating conditions are the same for both sets of measurements with $P_0 = 3.72$ atm and $P_1 = 1$ atm ($P_1/P_0 = 0.27$). The geometries are different.

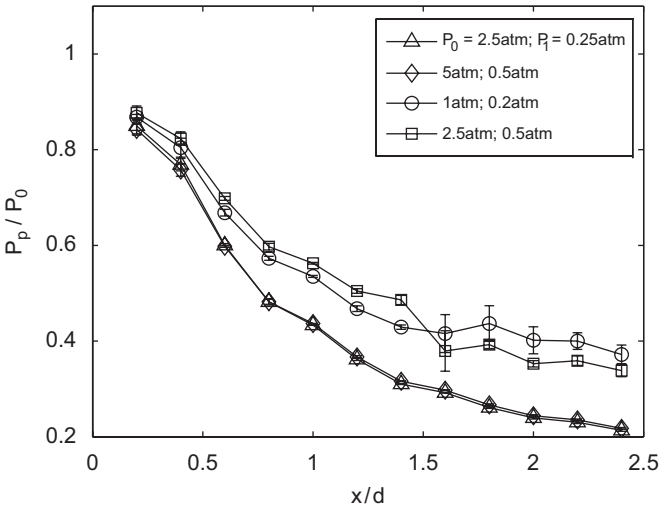

Fig. 3. Two sets of two Pitot pressure measurements in the developed impactor system presented as a function of x/d for different upstream and downstream pressures; the ratio, P_1/P_0, remains fixed. (Set 1) $P_1/P_0 = 0.1$ with $(P_0(\text{atm}), P_1(\text{atm})) = \{(2.5, 0.25), (5.0, 0.50)\}$, and (set 2) $P_1/P_0 = 0.2$ with $(P_0(\text{atm}), P_1(\text{atm})) = \{(1.0, 0.20), (2.5, 0.50)\}$.

thereby avoiding impinging flow. Due to this fact, in the experimental x/d range shown in Fig. 2, Powell's data have two maxima and one minimum whereas in the experimental measurements of the impactor system such a behavior is not observed. Both measurements though predict Mach numbers that are in the same range, i.e. M_1 is between 1 and 2.75 (see Fig. 2).

In the experimental impactor system of Fig. 1, more measurements were done with geometries of varying plate to nozzle distance ($0.2 < x/d < 2.4$; limited only by the spacer thicknesses) at different upstream ($1.0\,\text{atm} < P_0 < 8.9\,\text{atm}$) and downstream pressures ($0.12\,\text{atm} < P_1 < 0.9\,\text{atm}$). We compared measurements of P_p/P_0 at constant P_1/P_0 for different upstream and downstream pressures. In Fig. 3, the P_p/P_0 measurements are identical for equal P_1/P_0 with different upstream pressures. These results indicate that the main variable determining the ratio, P_p/P_0, is the upstream to downstream

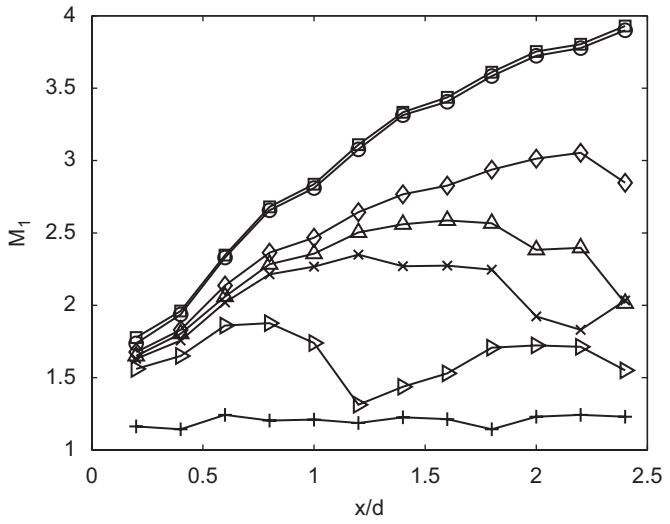

Fig. 4. Experimental Mach number before the shock (M_1) in the impactor system of Fig. 1 calculated using Eq. (4) as a function of x/d. Curves represent different operating conditions, represented by the downstream to upstream pressure ratio, P_1/P_0. $[P_1/P_0, P_0, P_1] = (\square)$ [0.05, 8.5, 0.4 atm] $(\bigcirc)$ [0.05, 5, 0.25 atm] $(\diamond)$ [0.16, 2.5, 0.4 atm] $(\triangle)$ [0.27, 3.72, 1 atm] $(\times)$ [0.25, 1, 0.25 atm] $(\triangleright)$ [0.32, 1, 0.32 atm], $(+)$ [0.50, 1, 0.5 atm].

pressure ratio instead of the absolute values of the pressures. CFD results further confirm these observations (see Section 3.2).

Fig. 4 shows the variation of the Mach number (M_1) with x/d for different P_1/P_0. The Mach number increases with decreasing P_1/P_0 and this trend is more pronounced at higher x/d ($x/d > 1$) which is observed in the computational results shown in Section 3.2 (see Fig. 9a). Fig. 4 reenforces the findings of Fig. 3 in that measurements made with the same P_1/P_0 but different P_0 and P_1 yield similar curves. Specifically, the calculated M_1 for $P_1/P_0 = 0.05$ is identical for two upstream pressures $P_0 = 8.5$ and 5 atm. The highest Mach number, calculated using Eq. (4), with the current setup was $M_1 = 3.93 \pm 0.01$ at $P_0 = 8.93 \pm 0.01$ atm, $P_1 = 0.41 \pm 0.01$ atm ($P_1/P_0 = 0.05$) and $x/d = 2.4$. The errors in the measurements are computed using the standard deviation of three independent Pitot measurements and are on the order of 0.01 atm. These measurements, along with the CFD predictions, are essential in understanding the key parameters that influence bacterial aerosol neutralization.

3.2. Computational results: gas flow and thermal fields

For the two-phase aerosol flow (air–bacteria) present in the impactor system, the equations for gas and particle dynamics are coupled. At low aerosol concentrations, however, the particle dynamics can be assumed to have no effect on the gas flow field (Friedlander, 2000), and the equations of particle velocity and temperature can be decoupled from those of the gas phase. The gas dynamics can therefore be solved independently and the results are then used to determine the particle trajectories (see Section 4). An Eulerian approach is used to solve the gas flow field. Because the flow is turbulent, a full solution to the Navier–Stokes equations requires a computationally intensive direct numerical simulation (DNS). In this work, the Reynolds-averaged Navier–Stokes (RANS) equations are solved so that the small-scale turbulences do not have to be simulated directly. In Reynolds averaging, variables such as velocity, pressure and energy are decomposed into a mean and fluctuating components as follows:

$$\phi = \overline{\phi} + \phi' \quad \text{with } \overline{\phi} = \frac{1}{\Delta t}\int_{t_0}^{t_0+\Delta t} \phi\, dt \text{ and } \overline{\phi'} = 0, \tag{7}$$

where ϕ is a scalar property of the fluid (e.g., velocity magnitude, pressure, temperature, energy), and $\overline{\phi}$ is the time-averaged component of ϕ with the corresponding fluctuating component ϕ'. If we substitute the above form for the flow variables into the instantaneous Navier–Stokes equations and take a time average, we obtain the equations that describe the gas flow field. For simplicity and to provide an idea of the terms included in these equations, we provide the general form of these equations in Cartesian tensor form (after dropping the overbars):

$$\frac{\partial \rho}{\partial t} + \frac{\partial}{\partial x_j}(\rho v_j) = 0 \tag{8}$$

and

$$\frac{\partial}{\partial t}(\rho v_i) + \frac{\partial}{\partial x_j}(\rho v_i v_j) = -\frac{\partial p}{\partial x_i} + \frac{\partial}{\partial x_j}\left[\mu\left(\frac{\partial v_i}{\partial x_j} + \frac{\partial v_j}{\partial x_i} - \frac{2}{3}\delta_{ij}\frac{\partial v_l}{\partial x_l}\right)\right] + \frac{\partial}{\partial x_j}(-\rho\overline{v_i' v_j'}), \quad i=1,2,3, \tag{9}$$

where ρ is the density, v is the velocity, p is the static pressure, δ is the Kronecker delta, μ is the viscosity, and i,j, and l are the indices. To close the form in Eq. (9), the Reynolds stress term $-\rho\overline{v_i' v_j'}$ is calculated using the Boussinesq hypothesis (Hinze, 1975):

$$-\rho\overline{v_i' v_j'} = \mu_t\left(\frac{\partial v_i}{\partial x_j} + \frac{\partial v_j}{\partial x_i}\right) - \frac{2}{3}\left(\rho k + \mu_t\frac{\partial v_l}{\partial x_l}\right)\delta_{ij}, \tag{10}$$

where μ_t is the turbulent viscosity and k is the turbulent kinetic energy. Different turbulence models were employed and compared giving similar results (see Remark 1). Neglecting the effect of gravity, the turbulence model used is the standard $k-\varepsilon$ model which is given by

$$\frac{\partial}{\partial t}(\rho k) + \frac{\partial}{\partial x_i}(\rho v_i k) = \frac{\partial}{\partial x_j}\left[\left(\mu + \frac{\mu_t}{\sigma_k}\right)\frac{\partial k}{\partial x_j}\right] + G_k - \rho\varepsilon - Y_M \tag{11}$$

and

$$\frac{\partial}{\partial t}(\rho\varepsilon) + \frac{\partial}{\partial x_i}(\rho v_i \varepsilon) = \frac{\partial}{\partial x_j}\left[\left(\mu + \frac{\mu_t}{\sigma_\varepsilon}\right)\frac{\partial \varepsilon}{\partial x_j}\right] + C_{1\varepsilon}\frac{\varepsilon}{k}(G_k + C_{3\varepsilon}G_b) - C_{2\varepsilon}\rho\frac{\varepsilon^2}{k},$$
$$\mu_t = \rho C_\mu \frac{k^2}{\varepsilon},$$
$$C_{1\varepsilon} = 1.44, \quad C_{2\varepsilon} = 1.92, \quad C_\mu = 0.09, \quad \sigma_k = 1.0, \quad \sigma_\varepsilon = 1.3, \tag{12}$$

where ε is the rate of dissipation, and G_k is the generation of turbulent kinetic energy due to mean velocity gradients. σ_k and σ_ε are the turbulent Prandtl numbers. Y_M is the dilatation dissipation term, which represents the contribution of the fluctuating dilatation in compressible turbulence to the overall dissipation rate. Y_M is given by

$$Y_M = 2\rho\varepsilon M_t^2, \tag{13}$$

where M_t is the turbulent Mach number, defined as

$$M_t = \sqrt{k/s^2}, \tag{14}$$

where s $(=\sqrt{\gamma RT})$ is the speed of sound and γ $(=c_p/c_v)$ is the ratio of specific heat. The final conservation law solved is the energy equation for the gas which is given, in Cartesian tensor form, as follows:

$$\frac{\partial}{\partial t}(\rho E) + \frac{\partial}{\partial x_i}[v_i(\rho E + p)] = \frac{\partial}{\partial x_j}\left[\alpha c_{p_g}(\mu+\mu_t)\frac{\partial T}{\partial x_j} + v_i(\mu+\mu_t)\left(\frac{\partial v_j}{\partial x_i} + \frac{\partial v_i}{\partial x_j} - \frac{2}{3}\delta_{ij}\frac{\partial v_l}{\partial x_l}\right)\right], \tag{15}$$

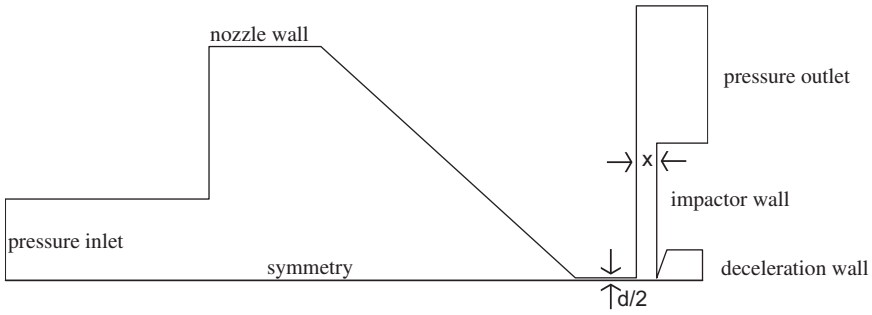

Fig. 5. Computational domain and boundary conditions.

Table 1
Inlet and outlet pressure conditions for parametric analysis of the impactor system with variable nozzle to plate distance (x/d).

Case	x/d (min:increment:max)	P_0 (atm)	P_1 (atm)	P_1/P_0	$(x/d)_c$
1 (base)	(0.2:0.1:4.0)	1.00	0.14	0.14	1.5
2	(0.2:0.1:2.4)	1.00	0.25	0.25	0.9
3	(0.2:0.1:2.4)	1.00	0.32	0.32	0.9
4	(0.2:0.1:2.4)	5.00	0.70	0.14	1.6
5 (for comparison)	(0.2:0.1:2.4)	3.72	1.00	0.27	–

$(x/d)_c$ refers to the value of x/d where instabilities in the flow arise.

where E is the internal energy, α is the thermal diffusivity, c_{p_g} is the heat capacity at constant pressure, and T is the static temperature.

A numerical solution program was written within FLUENT®, a CFD software, to solve the above equations for the computational domain shown in Fig. 5. Because the impactor is axisymmetric, a cross-sectional grid that covers half of the impactor system is used. A different mesh is created for different distances between the nozzle and the impactor wall (x/d). The distance shown in Fig. 5 is $x/d = 4.0$ with a nozzle diameter of 0.5 mm. The grid is more dense (0.01 mm without adaption; 0.0025 mm with adaption) in the area between the nozzle outlet and the deceleration tube inlet in order to capture the details of the shock. Both the inlet and the outlet boundaries are defined by stagnation pressures fixed at the values shown in Table 1 and temperatures fixed at 300 K with the gas considered to be ideal. The walls are defined by zero heat flux (adiabatic) and no-slip boundary conditions. As for the centerline, we use axisymmetric boundary conditions. Full multi-grid (FMG) initialization is used with the first-order upwind scheme to obtain a convergent solution to the momentum equation. Next, the energy and turbulence equations are solved with a first-order scheme followed by a second-order upwind scheme to obtain convergent solutions with residuals of continuity, velocity, k and ε of less than 10^{-4} and energy residual of less than 10^{-6}. Subsequently, three grid adaptation steps are applied to refine the mesh in areas with high pressure gradients, specifically in the area between the nozzle exit and the deceleration tube inlet. Li et al. (2004) and Li and Christofides (2003, 2005, 2006) used a similar approach to solve for a high velocity oxygen-fuel (HVOF) thermal spray process involving a converging–diverging nozzle.

A parametric study with different upstream and downstream pressures (see Table 1) is conducted to compare with the experimentally calculated Mach numbers (see Figs. 8 and 9) as well as to understand the effects of shocks with different properties on the bacterial aerosol. Cases 1 and 4 listed in Table 1 have different upstream pressures as boundary conditions; however, the ratio P_1/P_0 is constant. Case 5 is for comparison with experimental conditions that are similar to Powell (1988).

Theoretical and experimental observations indicate the presence of instabilities in the flow structure of the impinging jets in the presence of an impaction plate (Alvi et al., 2002; Jurcik et al., 1989; Powell, 1988). Understanding of the properties of an under-expanded free (absence of impaction plate) jet is essential for the study of instabilities for an impinging jet (Powell, 1988). In a free jet, as the flow emerges from the nozzle, it expands and accelerates to supersonic velocities creating a shock after which the gas velocity is subsonic (Powell, 1988). The subsonic flow expands further to regain sonic velocity thereby matching the nozzle conditions (Powell, 1988). The aerodynamic cell length is defined as the length of the region between the nozzle exit and the point where the free jet flow regains a near nozzle state. Instabilities in the flow structure (e.g., recirculation bubbles) arise when an impingement plate is placed at a distance equal to an aerodynamic cell length from the nozzle (Powell, 1988). Jurcik et al. (1989) computationally observed these instabilities by solving the time-dependent Navier–Stokes equations for $P_1/P_0 = 0.16$ at $x/d > 1.7$. Recirculation bubbles in the impingement zone, which lies at the center of the flow field between the shock and the plate, are an indication of instabilities (Alvi et al., 2002; Jurcik et al., 1989). Further study of the structure of the instabilities is outside the scope of this work; however, calculating the critical x/d $[(x/d)_c]$ at which instabilities arise, using the developed computational fluid dynamics model, is important in analyzing the particle motion in the impactor system (see Section 4). Further analysis of the flow structure for $P_0 = 1$ atm and $P_1 = 0.14$ atm ($P_1/P_0 = 0.14$) reveals the appearance of recirculation bubbles at $x/d > 1.5$, which is consistent with the range $x/d > 1.7$ reported by Jurcik et al. (1989). The recirculation bubble velocities increase as x/d increases. As P_1/P_0 decreases recirculation bubbles form at lower x/d with lower velocities. Furthermore, as can be seen in Fig. 6, the shock structure evolves from shocks forming away from the centerline, to standoff shocks, to diamond shock. At $x/d \leqslant 0.5$, the shocks form away from the centerline along the impactor walls because the nozzle area is not the critical flow area. As x/d increases, a standoff shock forms perpendicular to the centerline with increasing Mach numbers. For $x/d > 2.0$, a shock diamond forms with a subsequent second shock. For the different operating conditions, our study will focus on $0.5 < x/d < (x/d)_c$ where the shock is stable and along the path that the particle follows to settle in the deceleration tube. Table 1 refers to the $(x/d)_c$ values where instabilities arise for all the operating conditions studied.

The centerline properties of the fluid are typical of the flow field that a particle experiences before settling on the collection plate for analysis. In Section 4 the particle is released at the centerline. Therefore, the study will focus on the centerline properties of the complex flow field that develops in the experimental impactor of Fig. 1. Fig. 7 shows both the contour and the centerline temperature, pressure and Mach numbers for $x/d = 1.5$, $P_0 = 1$ atm and $P_1 = 0.14$ atm. As the gas exits the nozzle at 0.062 m from the impactor's in-

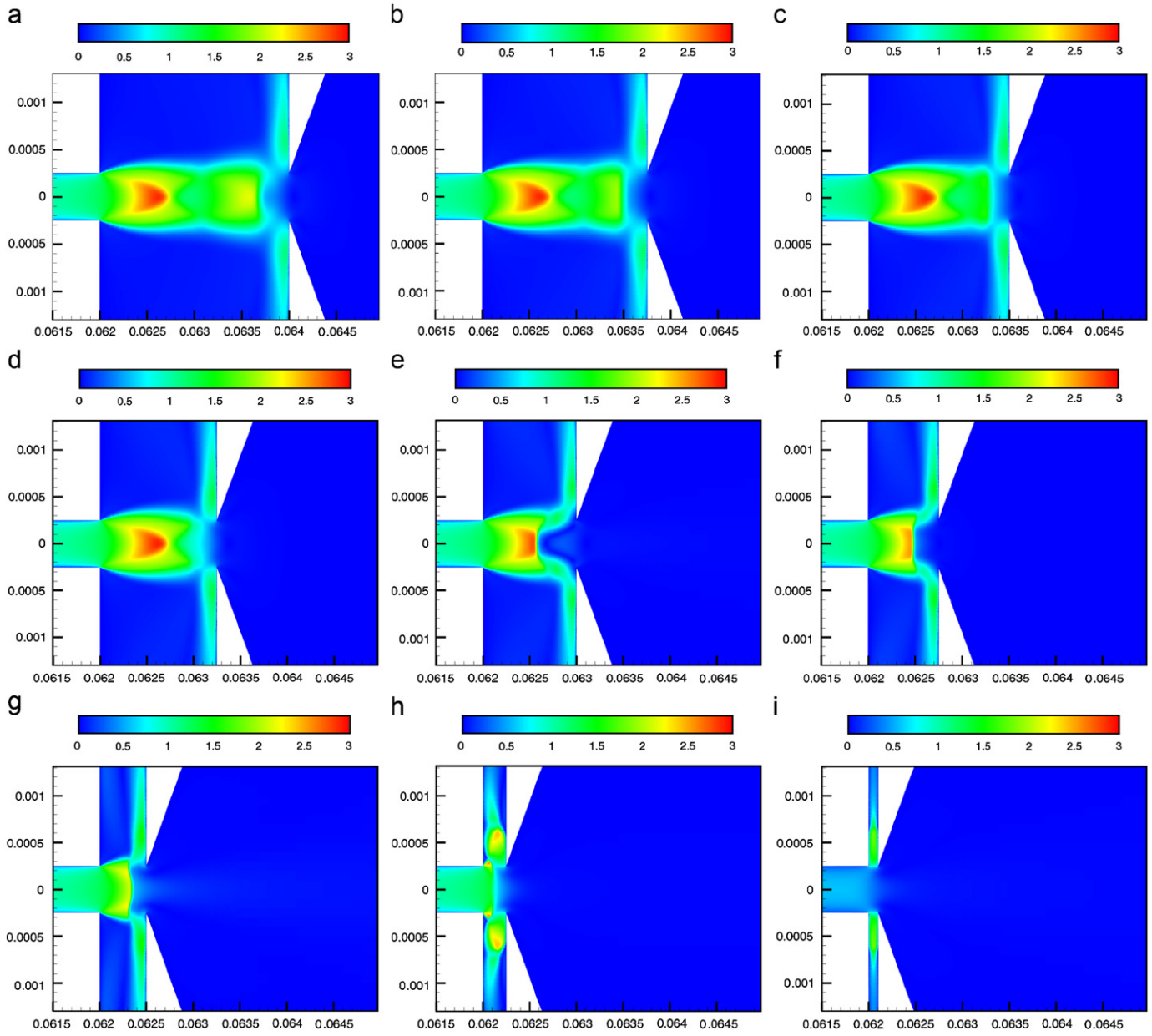

Fig. 6. Contour plots of the Mach number at different x/d for $P_0 = 1$ atm and $P_1 = 0.14$ atm. The x-axis is the distance along the centerline from the impactor inlet and is given in meters.

let, it expands reaching supersonic velocities before the shock. Correspondingly the static temperature and pressure decrease as the gas expands. In Fig. 7, the shock at 0.0625 m is observed as a sharp change in the fluid properties, which is responsible for the forces experienced by the bacteria (see Sections 4 and 5). In the contour plots of Mach, temperature and pressure, a standoff shock perpendicular to the direction of the flow can be observed. The Mach contour pattern is similar to the ones observed in experimental shadow graphs and wave diagrams in the literature (Alvi et al., 2002; Jurcik et al., 1989).

In the CFD model, the Pitot pressure is the centerline static pressure at the end of the deceleration tube (see Remark 3). The CFD calculations are made using idealized assumptions, discussed above, such as perfect gas, axisymmetric flow, and frictionless walls, whereas, in the experimental Pitot measurements these assumptions are not made and the pressure is measured directly. Therefore, we expect differences in the measured and computed values of the Pitot pressure. In Fig. 8a, the computational results yield higher Pitot pressures. However, the extracted maximum centerline Mach numbers represent a more accurate picture of the gas dynamics; specifically, at $x/d < 0.5$. Eq. (4) is for supersonic Pitot pressure measurements and does not account for subsonic conditions. At $x/d < 0.5$ the flow along the centerline is subsonic as discussed above (see Fig. 6). Therefore, Eq. (4), which yields Mach numbers > 1 at $x/d < 0.5$, is not accurate. Eq. (4) also does not take into account the formation of two shocks (see Fig. 6) after certain x/d giving rise to additional errors at higher x/d.

Even though a perfect match is not expected as discussed above, the trends in the computational maximum centerline Mach numbers are similar to the experimental results calculated using Eq. (4) as shown in Fig. 9a. The Mach number increases with decreasing P_1/P_0 and the effect is more pronounced after x/d of about 1. For the same upstream to downstream pressure ratio with different absolute values for the pressures, the maximum centerline Mach number

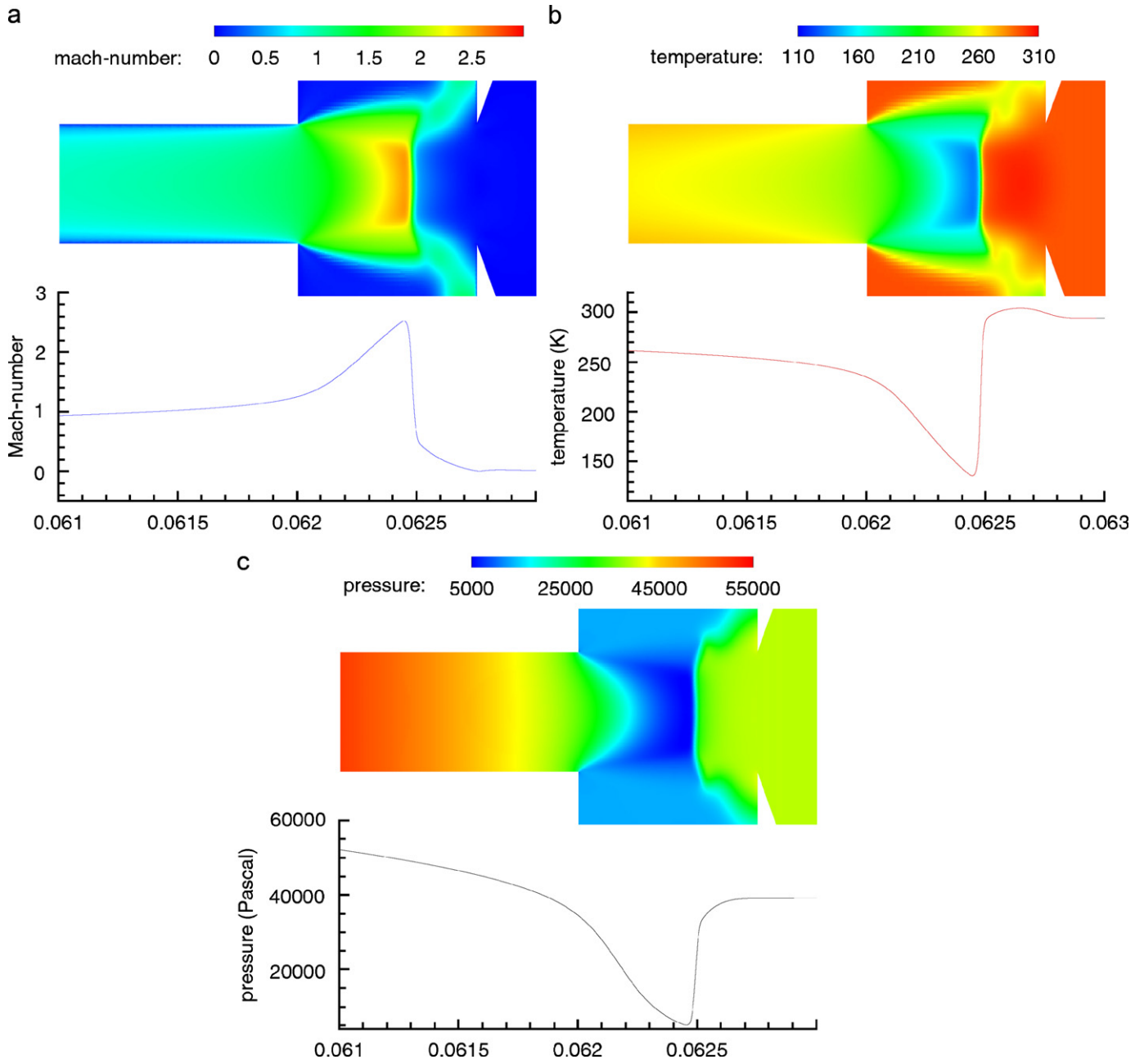

Fig. 7. Contour plots (top plots) and centerline fluid properties (bottom plots) for (a) Mach number, (b) static temperature and (c) static pressure. The x-axis is the distance along the centerline from the impactor inlet and is given in meters. The impactor is simulated at $x/d = 1.5$ with $P_0 = 1$ atm and $P_1 = 0.14$ atm.

is identical (see Fig. 9b). This fact is also confirmed for Mach numbers calculated from the experimental Pitot measurements of Fig. 3 as well as the Mach numbers shown in Fig. 4.

Although temperature effects will not be considered in the discussion of the forces experienced by the particle (see Section 5), we acknowledge that this effect exists and will be the focus of further study. The minimum temperature on the centerline decreases as P_1/P_0 increases (see Fig. 10). For constant P_0/P_1, the minimum temperature is identical, mimicking the Mach trend of Fig. 9.

In summary, the computational and experimental gas flow field analysis yields similar trends as discussed above. The absolute values differ because of the assumptions in calculating the Mach number employed in the developed models. The more detailed CFD model will be used in determining the forces exerted on the bacterial particles as they travel through the experimental impactor system of Fig. 1.

Remark 1. The centerline stagnation pressures at the end of the deceleration tube (Pitot pressures) were compared using Spalart–Allmaras, standard k–ε, RNG k–ε, and realizable k–ε models and the results were found to have a maximum deviation of 4%. The operating conditions for the comparison were $x/d = 0.6$, $P_0 = 5.48$ atm and $P_1 = 0.08$ atm. Based on these results, the standard k–ε model was chosen in all the simulations discussed in the study.

Remark 2. As noted in Section 3.1, the shock thickness is on the order of the mean free path (λ) of the gas. In the simulation results shown in Fig. 7, the centerline velocity drop occurs over a range of

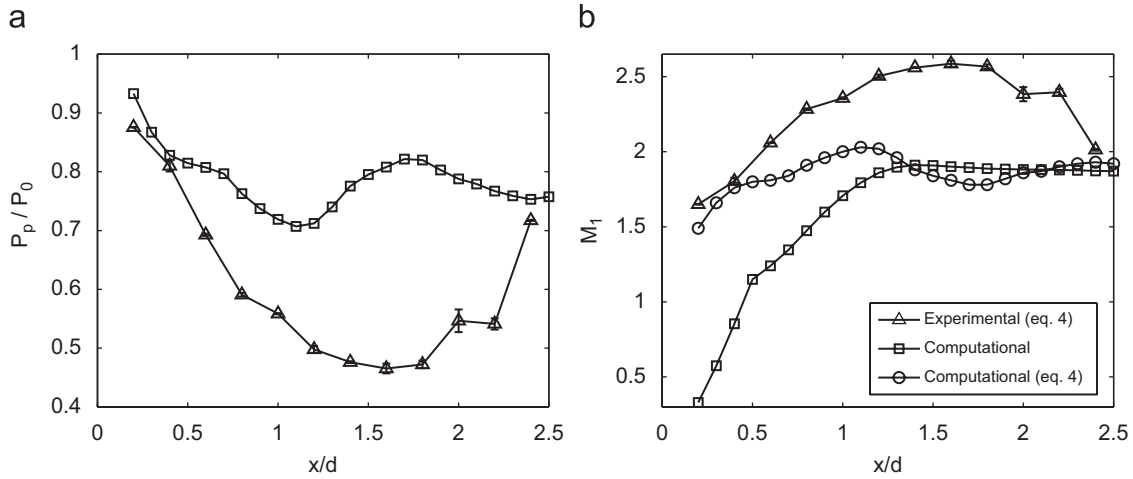

Fig. 8. (a) Pitot pressure versus x/d at $P_0 = 3.72$ atm and $P_1 = 1$ atm using both experimental and computational data of the experimental impactor system. It can be seen that the Pitot pressures are in agreement for very short distances but diverge as x/d increases. (b) Mach number versus x/d for the same conditions. (□) Maximum centerline Mach number extracted from computational gas dynamic model, (○) Mach number calculated using Eq. (4) and computational Pitot pressure data, (△) Mach number calculated using experimental Pitot pressure measurements.

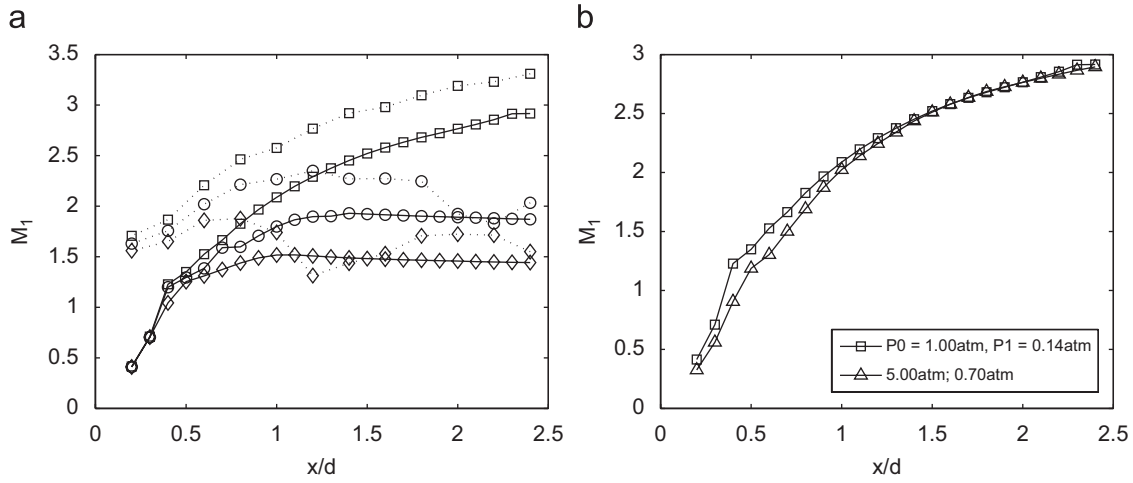

Fig. 9. (a) Computational (solid) versus experimental (dotted) maximum centerline Mach number (M_1) at different P_1/P_0: (□) $P_1/P_0 = 0.14$ (solid) and 0.15 (dotted), (○) 0.25, (⋄) 0.32. All the upstream pressures, P_0, are equal to 1. (b) Computational M_1 versus x/d at constant $P_1/P_0 = 0.14$ for different upstream and downstream pressures.

about 42 μm from a maximum Mach number of 2.52 to less than 1. The maximum mean free path along the centerline is 0.51 μm which is much less than the distance over which the Mach number decreases. CFD comparisons are based on flow equations that assume continuity and are therefore not able to capture non-continuum shock properties such as the shock thickness. However, this has a minimal effect on computing the forces acting on the bacterium as can be seen in Section 4.

Remark 3. All the reported computational Pitot pressures are extracted from static pressure data along the centerline and at the end of the deceleration tube. A new mesh was also created to capture the length of the Pitot tube (7 cm) of Figs. 1–7. Calculations using the new Mesh at $P_0 = 3.72$ atm, $P_1 = 1$ atm and $x/d = 1.6$ reveal a Pitot pressure equal to that at the end of the deceleration tube ($P_p = 3.00$ atm). The Pitot pressure is also equal by comparing the centerline pressure to the average pressure at the bottom of the deceleration tube. Therefore, reporting the centerline static pressure at the end of the deceleration tube is sufficient.

4. Bacterial motion in the impactor system

The bacterial motion in the impactor system is computed in Lagrangian coordinates utilizing the gas flow and temperature fields calculated using the CFD model of Section 3.2. Due to the very low bacterium loading, the coupling between the gas phase and the bacterial (particulate) phase can be considered to be one way, i.e. the gas flow field solution is obtained by neglecting the presence of bacteria and is subsequently used unmodified in the calculation of the bacterium trajectories. In the bacterium model development, it is also reasonable to assume that coagulation is negligible and that particle size does not change during flight.

The particle motion in the impactor system is governed by Newton's second law and is given by

$$m_p \frac{dv_p}{dt} = \sum_i F_i, \tag{16}$$

where m_p is the particle mass, v_p is the particle velocity, t is the time, and F_i represents the different forces that can act on the particle

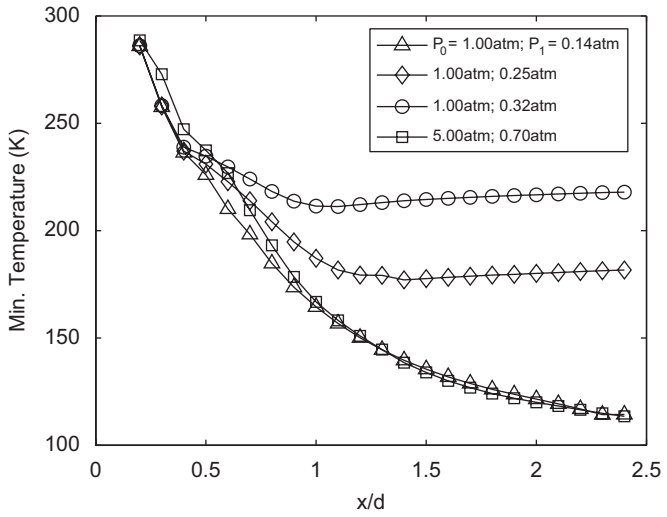

Fig. 10. Minimum centerline temperature of the gas as a function of the normalized distance between the nozzle and the plate (x/d) for four different (P_0, P_1) pairs.

including the drag force, thermophoretic force, gravitational force, and the basset history term. For typical impactor operating conditions, the major force acting on a bacterial particle is the drag force, and the other forces can be neglected. As a result, the force balance of Eq. (16) applied to bacterial particles traveling through the developed impactor system takes the following form:

$$m_p \frac{dv_p}{dt} = \frac{1}{2} C_D \rho_g A_p (v_g - v_p)|v_g - v_p|, \tag{17a}$$

$$\frac{dx}{dt} = v_p, \tag{17b}$$

where v_p and v_g are the velocity of the bacterial particle and gas, respectively, ρ_g is the density of the gas, A_p is the projected area of the bacterium on the plane perpendicular to the flow direction, and C_D is the drag coefficient. In the supersonic flows occurring in the impactor system, compressibility and non-continuum effects have to be considered in the evaluation of the drag coefficient C_D. Specifically, C_D is a function of both particle Reynolds ($Re_p = \rho_g d_p |v_g - v_p|/\mu_g$) and particle Mach ($Ma_p = |v_p - v_g|/s$; s is the speed of sound) numbers. For the simple case where the ratio of particle to gas absolute temperature, T_p/T_g, is approximately unity, data for $C_D = f(Re_p, Ma_p)$ are given in Clift et al. (1978). At each grid point the Re_p and Ma_p are computed and a corresponding value for C_D is evaluated.

The bacterial particle is assumed to be spherical at all times. The density (ρ_p) of bacterium is 1 mg/ml (Willeke and Baron, 2001). The dimension of bacterial particles varies depending on the species and the state of the individual bacterium. *B. subtilis*, for example, has a width of 0.7–0.8 μm and a length of 2–3 μm (Laskin and Lechevalier, 1974). Most bacteria diameters are in the micrometer range, and we will therefore assume that they are spheres of $d_p = 1$ μm for simplicity. The effect of particle size is discussed in Section 5.

It is also reasonable to assume that the bacterial particles are heated with negligible internal resistance and that the internal bacterial temperature gradient can be ignored due to the small Biot number (ratio of heat transfer coefficient due to the boundary layer versus the internal heat conductance; see Remark 4 for a detailed analysis of this issue). The mass of the particle, m_p, is constant. Therefore, we can model the evolution of the bacterial temperature accounting for the heat transfer between the particle and the gas with the following first-order ordinary differential equation:

$$m_p c_{p_p} \frac{dT_p}{dt} = h A'_p (T_g - T_p), \tag{18}$$

where c_{p_p} is the particle heat capacity at constant pressure and A'_p is the surface area of the particle. The heat transfer coefficient (h) is computed using the Ranz and Marshall correlation (Ranz and Marshall, 1952a,b)

$$h = \frac{k_g}{d_p}[2 + 0.6 Re_p^{1/2} Pr^{1/3}], \tag{19}$$

where k_g is the thermal conductivity of the gas and Pr is the Prandtl number ($Pr = c_{p_g}\mu_g/k_g$). The thermodynamic properties of the bacterium are extracted from Datta (2002).

A fifth-order Runge–Kutta method is used to numerically integrate Eqs. (17a), (17b) and (18) using the gas velocity and temperature fields obtained from the computational model of Section 3.2. The particle velocity and temperature are calculated every 10^{-7}m along the centerline of the impactor. These solutions are calculated for all conditions shown in Table 1, including flow fields where instabilities are seen (see Remark 5).

Compared to the maximum gas Mach (M_1) shown in Fig. 9a, the maximum particle Mach number ($Ma_p = \max|v_p - v_g|/s$; s is the speed of sound) does not exhibit a clear trend versus x/d (see Fig. 11a). Ma_p is approximately equal for different operating conditions up to $x/d \approx 0.8$. There is a peak that occurs for $P_0 = (1.00$ atm and $P_1 = 0.25$ atm) at $x/d \approx 1.1$. This might be because of the effect of the instabilities (see Remark 5 for a discussion on this issue). At higher x/d, the pressure pairs (P_0, P_1)=(1.00 atm, 0.14 atm) and (5.00 atm, 0.70 atm) have higher particle Mach numbers similar to the gas Mach number; however, these are at x/d values that exhibit instabilities. The minimum centerline particle temperature variation versus x/d of Fig. 11b is similar to the temperature variation of the gas phase in Fig. 9b. For equal ratio of P_1/P_0 the centerline particle temperature drop is higher for higher P_0. Therefore, although the gas flow and temperature are constant at constant P_1/P_0, the different absolute values of P_0 and P_1 affect the bacterial motion and temperature in the impactor system. Figs. 12 and 13 show the particle and gas velocity profiles as well as the mean free path as a function of the distance from the nozzle (x) for different operating conditions. In Fig. 12, x/d and P_0 are held constant at 1 and 1 atm, respectively, while P_1 assumes two values 0.14 and 0.25 atm. The mean free path is expected to be lower for $P_1 = 0.25$ atm and can be seen by comparing Figs. 12c and d. The instabilities in the flow can be seen in Fig. 12b where the centerline gas velocity assumes a negative velocity because of the recirculation bubble. The particle stops at the point where the gas velocity is zero (see Remark 5 for more details). In Fig. 13, x/d and P_1/P_0 are held constant at 1.4 and 0.14, respectively, while P_0 assumes two values 1 and 5 atm. Although the maximum centerline Mach numbers were the same for both cases (see Fig. 9a), the gas velocity drop and mean free path are different. The drop from maximum gas velocity to 100 m/s occurs over a length of 150 and 240 μm for $P_0 = 1$ and 5 atm, respectively. This will affect the forces experienced by the bacterial particles as they go through the impactor system (see Section 5).

Remark 4. The computational analysis of the impactor revealed a maximum Biot number of 0.31 ($x/d = 0.5$, $P_0 = 5$ atm and $P_1 = 0.7$ atm) using the following formula (Incropera and DeWitt, 2002)

$$Bi = \frac{h d_p}{6 k_p}, \tag{20}$$

where k_p is thermal conductivity of the bacterium and is given by Datta (2002) to be 0.44 W/mK. Although the maximum Biot in the parametric study is greater than 0.1, it is still well less than 1, and

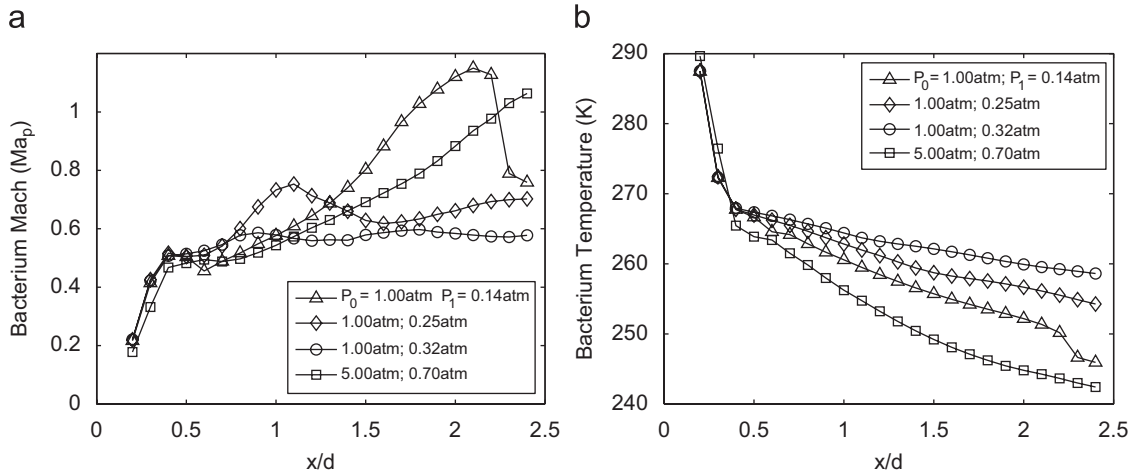

Fig. 11. (a) Maximum centerline particle Mach number and (b) minimum centerline temperature of the particle, as a function of the normalized distance between the nozzle and the plate (x/d) for four different (P_0, P_1) pairs.

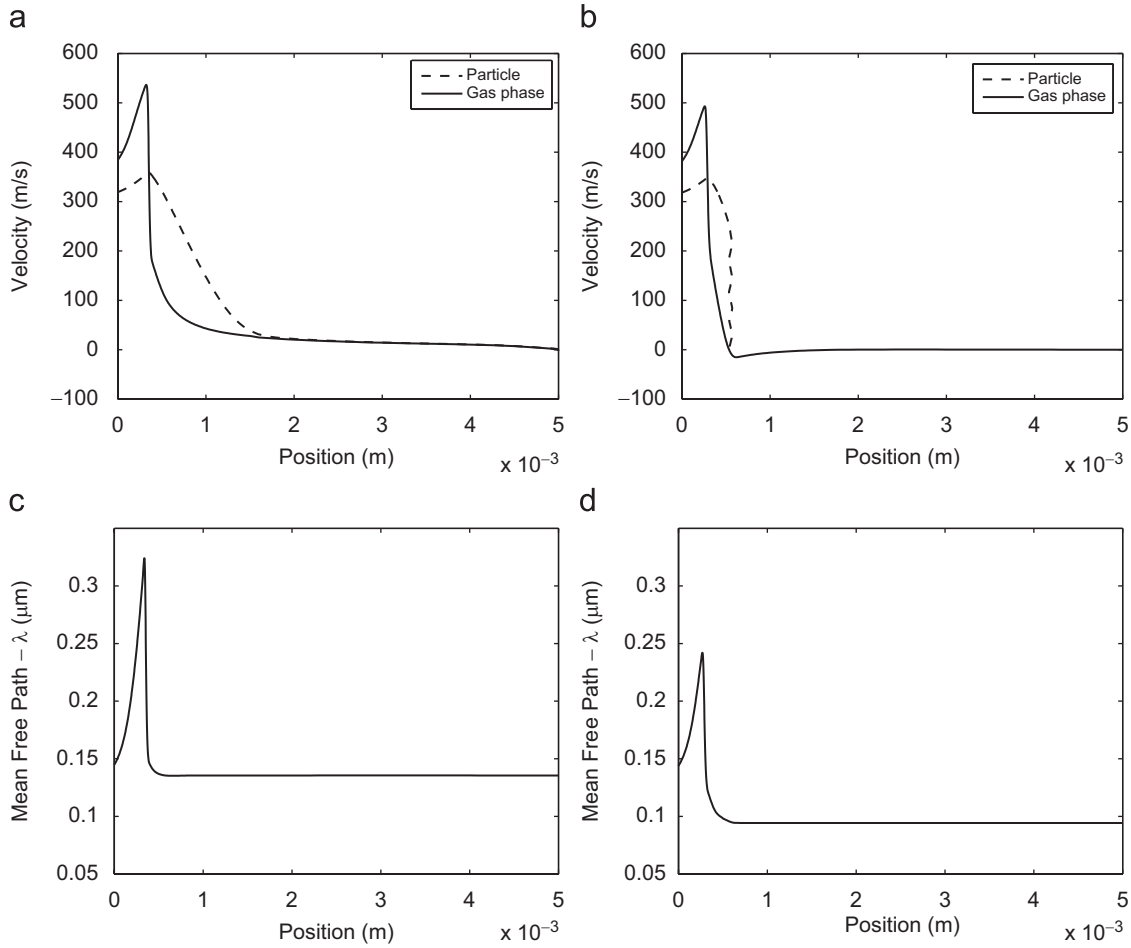

Fig. 12. (a, b) Centerline particle and gas velocity as a function of the distance from the nozzle. (c, d) Mean free path of the gas molecules as a function of distance along the centerline with 0 m marking the exit of the nozzle. Conditions: (a, c) $x/d = 1.0$, $P_0 = 1$ atm and $P_1 = 0.14$ atm, (b, d) $x/d = 1.0$, $P_0 = 1$ atm and $P_1 = 0.25$ atm.

thus Eq. (18) is a good approximation since the internal resistance to heat transfer is well less than the external one.

Remark 5. In the unstable flow conditions (i.e., the presence of recirculation bubbles in the flow field) discussed in Section 3.2, the use of Eqs. (17a) and (17b) does not capture the particle behavior in the experimental impactor system. Specifically, in this case, the computations reveal that the particles stop before reaching the collection plate and in some cases before entering the deceleration tube. This type of behavior arises because of the negative velocities of the gas on the centerline caused by the recirculation bubble. Furthermore, the particle motion (Eqs. (17a) and (17b)) does not account for forces

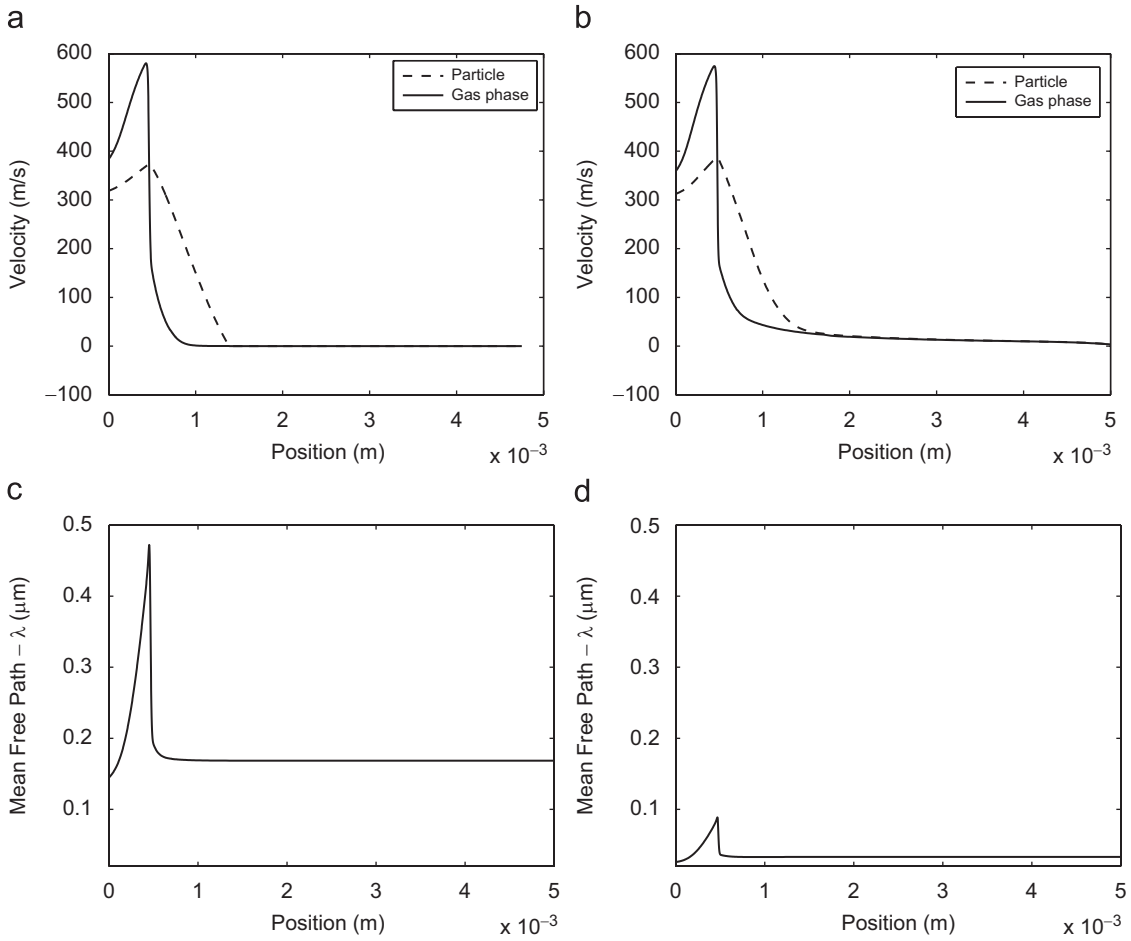

Fig. 13. (a, b) Centerline particle and gas velocity as a function of distance from the nozzle. (c, d) Mean free path of the gas molecules as a function of distance along the centerline with 0 m marking the exit of the nozzle. Conditions: (a, c) $x/d = 1.4$, $P_0 = 1$ atm and $P_1 = 0.14$ atm, (b, d) $x/d = 1.4$, $P_0 = 5$ atm and $P_1 = 0.70$ atm.

such as gravity, Brownian motion, and turbulent dispersion which may need to be included to improve the accuracy of the particle motion trajectory calculations at unstable flow conditions. The effects of Brownian motion and turbulent dispersion on the particle trajectories and accelerations will be the subject of future work. To study these forces more detailed simulations are necessary where a cloud of particles is released from the centerline and average properties are calculated.

5. Bacterial envelope instability

Instabilities in the bacterial membrane arise if the bacterial particle is accelerated (or decelerated) in a perpendicular direction to the bacteria–gas interface (direction parallel to the centerline x-direction) and are referred to as Rayleigh–Taylor instabilities (Chandrasekhar, 1961; Joseph et al., 1999). The relative acceleration creates waves in the surface of the bacteria with characteristic wavelengths. These waves can grow uncontrollably if not for the stabilizing effect of surface tension. However, once a critical wavelength is reached, surface tension cannot compensate for the growth of waves on the bacterial surface and the bacterium breaks up. This phenomenon has been studied extensively by Chandrasekhar (1961) and Joseph et al. (1999). Specifically, a bacterium is predicted to break up if

$$d_p > \lambda_c = 2\pi\sqrt{\frac{\sigma}{\rho_p a_c}}, \tag{21}$$

where λ_c is the critical wavelength and is directly related to the critical bacterial acceleration a_c. In Eq. (21), σ is the surface tension, ρ_p is the particle density and d_p is the particle diameter. Other conditions, which have to be satisfied for the critical acceleration to cause a break-up, are expressed in terms of two dimensionless numbers (Joseph et al., 1999). Specifically,

$$We > We_c = 12(1 + 1.077Oh^{1.6}), \tag{22}$$

where

$$We = \frac{\rho_g(v_{p_x} - v_{g_x})^2 d_p}{\sigma} \tag{23}$$

and

$$Oh = \frac{\mu_p}{(\rho_p d_p \sigma)^{1/2}}, \tag{24}$$

where We is the Weber number, which is the ratio between the inertial force exerted on the bacterial particle and the particle surface tension force. Oh refers to the Ohnesorge number, which is the ratio between the viscous forces and the surface tension force. v_{p_x} and v_{g_x} are the particle and gas velocity in the x-direction, respectively. We can therefore infer bacterial membrane break-up by computing the relative velocity $(v_{p_x} - v_{g_x})$ of the bacterium, as well as the maximum acceleration achieved. Since the particle grid and the gas grid do not coincide, the gas velocity is linearly interpolated to obtain data at the specific positions where the particle velocity is calculated.

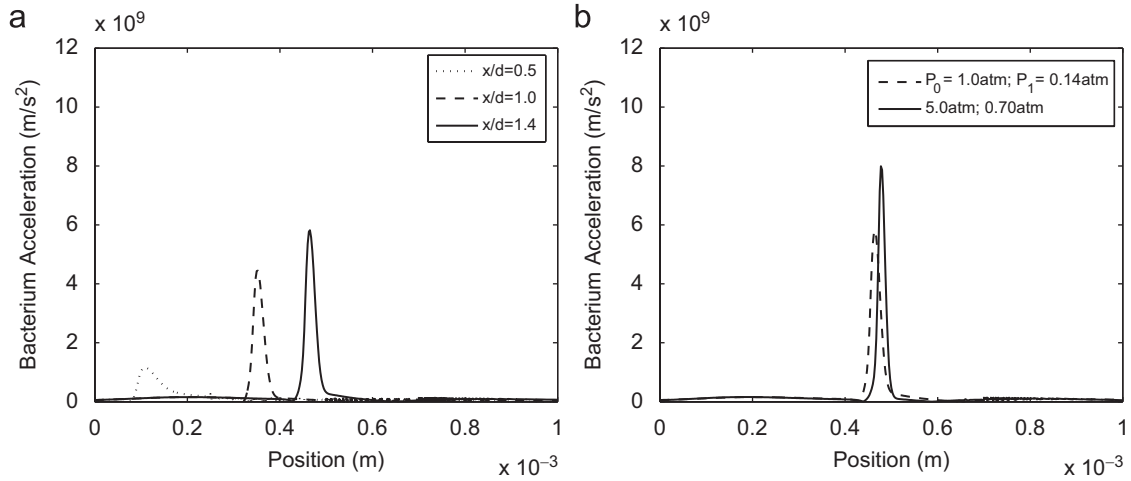

Fig. 14. Bacterial particle acceleration (relative to gas flow) as a function of distance from the nozzle outlet. (a) The operating conditions are constant for all three curves at $P_0 = 1$ atm and $P_1 = 0.14$ atm. The x/d varies for each case from 0.5 to 1.4. (b) The x/d is held constant at 1.4 as well as P_1/P_0 at 0.14. The acceleration is higher for the case where $P_0 = 5$ atm.

Table 2
Biological cell properties (Zinin et al., 2005) (not limited to bacteria) and critical shock properties needed to induce bacterial break-up.

Cell	d_p (μm)	σ (N/m)	a_c (m/s^2)	Oh	We_c	We_{max}
E. coli	1	7.5×10^{-3}	3.0×10^{8}	3.7×10^{-1}	1.4×10^{1}	2.9×10^{1}
D. carota	60	4.5×10^{1}	4.9×10^{8}	6.1×10^{-4}	1.2×10^{1}	3.0×10^{-1}
M. hungatei	0.44	$3.5 - 5$	$0.7–1.0 \times 10^{12}$	$2.1–2.5 \times 10^{-2}$	1.2×10^{1}	$2.0–2.8 \times 10^{-2}$
C. eugametos	16	3.8×10^{1}	5.9×10^{9}	1.3×10^{-3}	1.2×10^{1}	9.4×10^{-2}
B. Emersonii	20	3.2×10^{1}	3.2×10^{10}	1.3×10^{-3}	1.2×10^{1}	1.4×10^{-1}

The maximum Weber number is calculated for 1 μm particles (see Remark 6).

Specifically, the relative velocity is then numerically differentiated with respect to time to give the maximum acceleration as follows:

$$v_{g_{x_j}} = \frac{v_{g_{x_i}} - v_{g_{x_{i+1}}}}{t_i - t_{i+1}}(t_j - t_i) + v_{g_{x_i}}, \quad \forall t_j \in [t_i, t_{i+1}], \tag{25}$$

and

$$a_{max} = \max_j \left| \frac{(v_{g_{x_{j+1}}} - v_{p_{x_{j+1}}}) - (v_{g_{x_j}} - v_{p_{x_j}})}{t_{j+1} - t_j} \right|, \tag{26}$$

where i and j are the indices of gas and particle grid points, respectively, and t_i and t_j are the times at the grid points i and j, respectively. Only grid points between the nozzle exit and the deceleration tube entrance are considered in the calculation of the maximum acceleration in the x-direction.

Fig. 14 shows the acceleration of the bacterial particles relative to the gas stream. The bacterial envelope becomes unstable at a critical acceleration ($a_c = (4\pi^2\sigma)/(\rho_p d_p^2)$) which depends on the surface tension, density and diameter of the bacterium. The values of a_c for different bacteria are shown in Table 2 along with the Weber and Ohnesorg numbers. If the maximum calculated Weber number in the impactor system (We_{max}) exceeds the critical Weber number We_c, then conditions are satisfied to achieve bacterial break-up at the critical accelerations (a_c). Spores (i.e., properties similar to *M. hungatei*) have a higher surface tension (lower We_{max} and higher a_c) than vegetative cells (i.e., *E. coli*) and hence they are more difficult to damage mechanically. Table 2 indicates that all of the cells except *E. coli*, does not satisfy the critical Weber number requirement; basically, the cells do not achieve the energies needed for break-up. The computational results shown in Fig. 15 indicate that the maximum accelerations achieved in the developed experimental impactor system are on the order of 10^9–10^{10} m/s^2 including data for a wide range of x/d values. Comparing these data with the critical accelerations shown in Table 2, we can predict the possibility of break-up of certain bacterial particles in experimental impactor system. For example, *E. coli*, a vegetative gram-negative bacterium, requires an acceleration of 3.0×10^8 m/s^2 and we, therefore, predict that the experimental impactor is capable of neutralizing this bioaerosol. On the other hand *M. hugatei*, an archaea, which has properties close to *B. atropheus*, a spore forming gram-positive bacterium, requires an

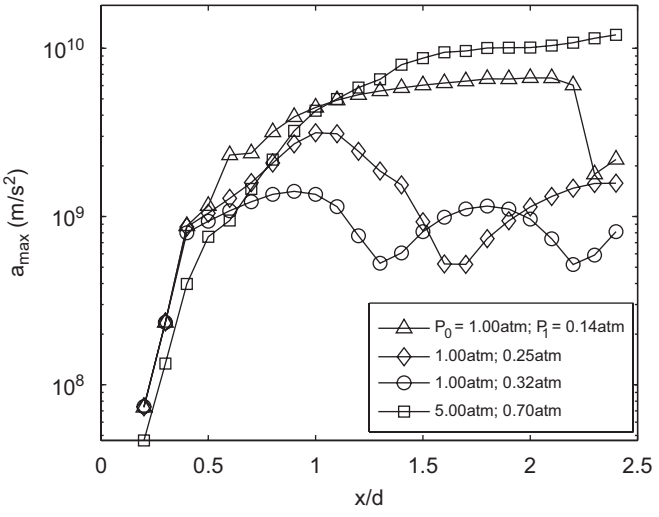

Fig. 15. Maximum centerline acceleration of the particle as a function of normalized distance between the nozzle and the plate (x/d) for four different (P_0, P_1) pairs.

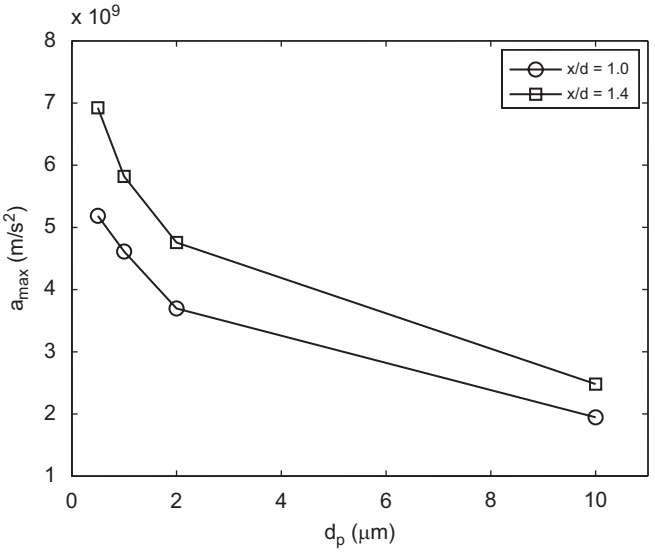

Fig. 16. Maximum centerline acceleration of the particle as a function of the particle size in impactor system operated at $P_0 = 1$ atm and $P_1 = 0.14$ atm for two values of x/d.

acceleration of 1.0×10^{12} m/s^2 which cannot be achieved by the developed experimental impactor system. We currently carry out experimental work with both vegetative cells and spores to verify the computational model predictions discussed above.

Remark 6. Particle size affects the relative velocity between the bacterial particle and the gas, which leads to a change in the Weber number. In this work, the Weber number of a 0.5 μm bacterial particle was compared to that of a 1.0 μm bacterial particle at $P_0 = 1$ atm, $P_1 = 0.14$ atm and $x/d = 1.4$. The difference in value was ≈ 5%, which is not significant considering that the maximum Weber number of *M. hungatei* ($d_p = 0.44$ μm) is much smaller than the critical one (see Table 2). The a_{max} values also change with different particle sizes as shown in Fig. 16. However, these changes are not significant since they are of the same order of magnitude.

6. Conclusions

Neutralization of bacterial aerosol releases is critical in countering bioterrorism. As a possible bacterial aerosol neutralization method that avoids the use of chemicals, we investigated the Rayleigh–Taylor instabilities of the bacterial cell envelope in air as the bacteria pass through aerodynamic shocks. To carry out this fundamental investigation, a novel experimental impactor system was designed and built to simultaneously create a controlled and measured shock, as well as to collect the bacteria after they pass through the shock. The system consists of a converging nozzle through which aerosol flows perpendicular to a collection surface that has an orifice through which the shocked bacteria enter the deceleration tube. For this impactor, a computational fluid dynamics model of the experimental impactor system of Fig. 1 was developed and used to predict the bacterial motion as they pass through the shock and are collected in the deceleration tube. Specifically, the developed computational model described the evolution of both the gas and the particle velocity and temperature in the impactor system. Experimental measurements of the pressure in the impactor system at multiple points followed the same trends as the computational fluid dynamics simulations. Our models predict that the bacterial accelerations achieved in the impactor system of Fig. 1 are on the order of $10^9 - 10^{10}$ m/s^2 for various conditions of x/d, P_0 and P_1, which are capable of neutralizing certain bacterial aerosols. Currently, we are carrying out experimental work to verify these predictions.

Notation

a_c	critical bacterial acceleration
A'_p	surface area of particle
Bi	Biot number
C_c	Cunningham slip correction factor
C_D	drag coefficient
c_{p_g}	heat capacity of gas at constant pressure
c_{p_p}	heat capacity of particle at constant pressure
d	nozzle diameter
d_p	particle diameter
E	internal energy
F_D	drag force
g	gravitational constant
h	heat transfer coefficient
k	turbulent kinetic energy
k_g	particle heat conductivity
m_p	particle mass
Ma_p	maximum particle Mach number
M_1	gas Mach number before shock
M_2	gas Mach number after shock
Oh	Ohnesorge number
p	static pressure of gas
p_{01}	stagnation (or total) pressure before shock
p_{02}	stagnation (or total) pressure after shock
P_p	Pitot stagnation pressure
Pr	Prandtl number
P_0	upstream stagnation pressure
P_1	downstream stagnation pressure
P_{01}	static pressure before shock
Re_p	particle Reynold's number
s	speed of sound
T/T_g	static temperature of gas
T_p	static temperature of particle
T_{01}	static temperature before shock
v/v_g	gas velocity
x	plate to nozzle distance
v_p	particle velocity
We	Webernumber
We_c	critical Weber number

Greek letters

α	thermal diffusivity
ε	rate of dissipation
γ	heat capacity ratio
λ	gas mean free path
μ/μ_g	dynamic viscosity of gas
μ_t	turbulent viscosity
ρ/ρ_g	gas density
ρ_p	particle density
σ	bacterial surface tension

Acknowledgments

This work has been supported by the Defense Threat Reduction Agency (DTRA) under grant number HDTRA1-07-0012. The authors would also like to acknowledge the late Prof. Sheldon K. Friedlander for initiating the project and for advising Patrick R. Sislian.

References

Alvi, F.S., Ladd, J.A., Bower, W.W., 2002. Experimental and computational investigation of supersonic impinging jets. AIAA Journal 40 (4), 599–609.

Biswas, P., Flagan, R.C., 1988. The particle trap impactor. Journal of Aerosol Science 19 (1), 113–121.

Bovallius, A., Bucht, B., Roffey, R., Anas, P., 1978. Three-year investigation of natural airborne bacterial-flora at four localities in Sweden. Applied and Environmental Microbiology 35 (5), 847–852.

Chandrasekhar S., 1961. Hydrodynamic and Hydromagnetic Stability, first ed. In: The International Series of Monographs on Physics, Clarendon Press, Oxford.

Clift, R., Grace, J.R., Weber, M.E., 1978. Bubbles, Drops, and Particles. Academic Press, New York.

Datta, A.K., 2002. Biological and Bioenvironmental Heat and Mass Transfer. Marcel Dekker, New York.

Delamora, J.F., Hering, S.V., Rao, N., McMurry, P.H., 1990a. Hypersonic impaction of ultrafine particles. Journal of Aerosol Science 21 (2), 169–187.

Delamora, J.F., Rao, N., McMurry, P.H., 1990b. Inertial impaction of fine particles at moderate Reynolds-numbers and in the transonic regime with a thin-plate orifice nozzle. Journal of Aerosol Science 21 (7), 889–909.

Di Giorgio, C., Krempff, A., Guiraud, H., Binder, P., Tiret, C., Dumenil, G., 1996. Atmospheric pollution by airborne microorganisms in the city of Marseilles. Atmospheric Environment 30 (1), 155–160.

Donaldson, C.D., Snedeker, R.S., 1971. Study of free jet impingement. 1. Mean properties of free and impinging jets. Journal of Fluid Mechanics 45 (2), 281–319.

Friedlander S.K., 2000. Smoke, Dust, and Haze: Fundamentals of Aerosol Dynamics, second ed. In: Topics in Chemical Engineering, Oxford University Press.

Hering, S.V., Flagan, R.C., Friedlander, S.K., 1978. Design and evaluation of new low-pressure impactor. 1. Environmental Science and Technology 12 (6), 667–673.

Hering, S.V., Friedlander, S.K., Collins, J.J., Richards, L.W., 1979. Design and evaluation of a new low-pressure impactor. 2. Environmental Science and Technology 13 (2), 184–188.

Hinze J.O., 1975. Turbulence, second ed. In: McGraw-Hill Series in Mechanical Engineering, McGraw-Hill, New York.

Horneck, G., Stoffler, D., Eschweiler, U., Hornemann, U., 2001. Bacterial spores survive simulated meteorite impact. Icarus 149 (1), 285–290.

Incropera, F.P., DeWitt, D.P., 2002. Fundamentals of Heat and Mass Transfer. fifth ed.. Wiley, New Jersey.

Jones, B.L., Cookson, J.T., 1983. Natural atmospheric microbial conditions in a typical suburban area. Applied and Environmental Microbiology 45 (3), 919–934.

Joseph, D.D., Belanger, J., Beavers, G.S., 1999. Breakup of a liquid drop suddenly exposed to a high-speed airstream. International Journal of Multiphase Flow 25 (6–7), 1263–1303.

Jurcik, B.J., Brock, J.R., Trachtenberg, I., 1989. A study of low-pressure particle impaction processes. Journal of Aerosol Science 20 (6), 701–711.

Laskin A.I., Lechevalier H.A., 1974. CRC Handbook of Microbiology, vol. 1, CRC Press.

Li, M.H., Christofides, P.D., 2003. Modeling and analysis of HVOF thermal spray process accounting for powder size distribution. Chemical Engineering Science 58 (3–6), 849–857.

Li, M.H., Christofides, P.D., 2005. Multi-scale modeling and analysis of an industrial HVOF thermal spray process. Chemical Engineering Science 60 (13), 3649–3669.

Li, M.H., Christofides, P.D., 2006. Computational study of particle in-flight behavior in the HVOF thermal spray process. Chemical Engineering Science 61 (19), 6540–6552.

Li, M.H., Shi, D., Christofides, P.D., 2004. Diamond jet hybrid HVOF thermal spray: gas-phase and particle behavior modeling and feedback control design. Industrial and Engineering Chemistry Research 43 (14), 3632–3652.

Liepmann, H.W., Roshko, A., 2001. Elements of Gasdynamics. Dover Publications, Dover Books on Engineering.

Lighthart, B., Shaffer, B.T., 1997. Increased airborne bacterial survival as a function of particle content and size. Aerosol Science and Technology 27 (3), 439–446.

Lundbeck, H., Skoldber, O., 1963. Effect of pressure waves on bacteria suspended in water. Biotechnology and Bioengineering 5 (3), 167–184.

Mancinelli, R.L., Shulls, W.A., 1978. Airborne bacteria in an urban environment. Applied and Environmental Microbiology 35 (6), 1095–1101.

Powell, A., 1988. The sound-producing oscillations of round underexpanded jets impinging on normal plates. Journal of the Acoustical Society of America 83 (2), 515–533.

Ranz, W.E., Marshall, W.R., 1952a. Evaporation from drops. 1. Chemical Engineering Progress 48 (3), 141–146.

Ranz, W.E., Marshall, W.R., 1952b. Evaporation from drops. 2. Chemical Engineering Progress 48 (4), 173–180.

Scroggs, S.D., Settles, G.S., 1996. An experimental study of supersonic microjets. Experiments in Fluids 21 (6), 401–409.

Shaffer, B.T., Lighthart, B., 1997. Survey of culturable airborne bacteria at four diverse locations in Oregon: urban, rural, forest, and coastal. Microbial Ecology 34 (3), 167–177.

Shapiro, A.H., 1953. The Dynamics and Thermodynamics of Compressible Fluid Flow. The Ronald Press Company, New York.

Stewart, S.L., Grinshpun, S.A., Willeke, K., Terzieva, S., Ulevicius, V., Donnelly, J., 1995. Effect of impact stress on microbial recovery on an agar surface. Applied and Environmental Microbiology 61 (4), 1232–1239.

Teshima, K., Ohshima, T., Tanaka, S., Nagai, T., 1995. Biomechanical effects of shock-waves on *Escherichia coli* and lambda-phage DNA. Shock Waves 4 (6), 293–297.

Tong, Y.Y., Lighthart, B., 1999. Diurnal distribution of total and culturable atmospheric bacteria at a rural site. Aerosol Science and Technology 30 (2), 246–254.

Vitko, J., 2005. Sensor systems for biological agent attacks: protecting buildings and military bases. Technical Report, The National Academies Press.

Willeke, K., Baron, P.A., 2001. Aerosol Measurement: Principles, Techniques, and Applications. Wiley-Interscience, New York.

Zinin, P.V., Allen, J.S., Levin, V.M., 2005. Mechanical resonances of bacteria cells. Physical Review E 72 (6), 061907.1–061907.10.